Nonplanar trapezoidal tooth log-periodic antennas: Design and electromagnetic modeling

Özgür Ergül and Levent Gürel

Department of Electrical and Electronics Engineering, Bilkent University, Ankara, Turkey

Received 16 November 2004; revised 8 May 2005; accepted 20 June 2005; published 18 October 2005.

[1] Nonplanar trapezoidal tooth log-periodic (LP) antennas are investigated by combining the wisdom of theoretical design procedures with the power of accurate numerical simulation environments. Once the theoretical design is completed, electromagnetic simulations employing accurate integral equation solvers are utilized to test and correct the original design. A two-element array of trapezoidal tooth LP antennas is designed. The array features beam-steering ability as a novelty, in addition to frequency independence and higher directivity. Beam steering is achieved by optimizing the excitation coefficients of the two LP antennas.

Citation: Ergül, Ö., and L. Gürel (2005), Nonplanar trapezoidal tooth log-periodic antennas: Design and electromagnetic modeling, *Radio Sci.*, *40*, RS5010, doi:10.1029/2004RS003215.

1. Introduction

[2] Log-periodic (LP) antennas are important with their ability to display nearly frequency-independent characteristics over wide bands of frequency. This type of antenna has a long history since the late 1950s, when DuHamel and Isbell introduced the first log-periodic structures [*DuHamel and Isbell*, 1957; *Isbell*, 1958; *DuHamel and Ore*, 1958]. After that, further studies focused on improving the performance and geometric properties of the LP antennas, as well as developing and inventing novel structures, such as the LP dipole arrays introduced in 1960 [*Isbell*, 1960].

[3] LP dipole arrays have been very popular with their detailed analysis given by Carrel [*Carrel*, 1961] and developed later in various studies [*De Vito and Stracca*, 1973; *De Vito and Stracca*, 1974; *Butson and Thompson*, 1976; *Peixeiro*, 1988]. In those reports, the antenna problem is modelled by a network of mutually coupled dipoles. On the basis of Carrel's work, straightforward and widely accepted design procedures for the LP dipole arrays are readily available in many famous textbooks [*Stutzman and Thiele*, 1981; *Kraus*, 1988; *Balanis*, 1997] and well-known references [*DuHamel and Chadwick*, 1984; *Mayes*, 1988]. Those design recipes, which will not be repeated here for sake of brevity, have passed the test of time by providing remarkably successful solutions to the LP dipole array problem.

0048-6604/05/2004RS003215$11.00

[4] Geometric simplicity of the LP dipole arrays leads to an important advantage in terms of numerical modeling, which facilitates the investigations and simulations prior to their hardware realizations. Numerous reports introducing new analysis techniques for the LP dipole arrays [*Jones and Mayes*, 1969; *Wolter*, 1970; *Paul and Gupta*, 1981], investigating their operational properties [*Kyle*, 1970; *Gong and Balmain*, 1986; *Hilbert et al.*, 1989; *Baker and Reuss*, 1990; *Hassan et al.*, 1991], and developing novel configurations for improved performance [*Oakes and Balmain*, 1973; *Tranquilla and Balmain*, 1983; *Wakabayashi et al.*, 1999; *Excell et al.*, 1999] have appeared in the literature. The same degree of success has not been obtained in the study of other LP structures with more complicated geometries, resulting in relatively fewer reports of detailed analysis [*Bell et al.*, 1960; *Liang and Lo*, 1968; *Lee and Mei*, 1970; *Hall*, 1986; *Smith and Mayes*, 1991] based on measurements and approximate numerical techniques.

[5] In this paper, our goal is to focus on the nonplanar trapezoidal tooth LP antennas (Figure 1) and investigate their important features, such as, frequency independence, pattern, and directivity, both individually and in a two-element array environment. At the same time, we demonstrate that accurate numerical simulations can bridge the gap between the approximate designs of LP structures obtained with the theoretical design recipes and the more precise performance requirements. This kind of an improvement supplied by the simulation can be very valuable for LP antennas that have more complicated geometries than the LP dipole arrays [*Tammen*

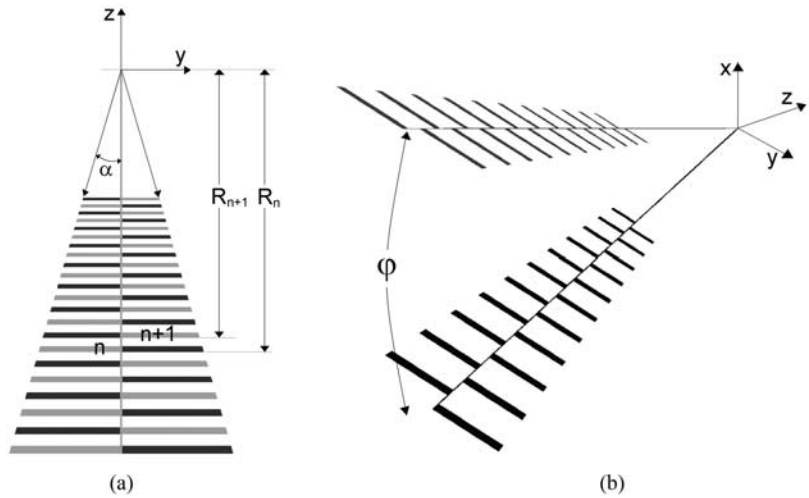

Figure 1. Trapezoidal tooth log-periodic antenna design: (a) top view and (b) three-dimensional view. One arm of the antenna is shown in black and the other one in gray.

et al., 1993]. Our simulation environment, which is described in section 2, is capable of handling arbitrary geometries, including complicated LP antennas. In section 3, we focus on the nonplanar trapezoidal tooth LP antennas due to genuine practical needs since this work is part of our pursuit of developing arrays of LP antennas with beam-steering ability [*Gürel and Ergül*, 2004]. Along this direction, frequency independence and beam-steering abilities of a two-element array of trapezoidal tooth LP antennas are also reported in section 3. Optimization of more populous arrays using genetic algorithms will be reported elsewhere [*Gürel and Ergül*, 2004]. To our knowledge, this is the first investigation of the beam-steering abilities of arrays of these broadband log-periodic antennas.

[6] It is imperative to note that the numerical results obtained by a blind use of the simulation environment cannot and should not replace the theoretical and analytical design procedures. Simulation results can provide improvements only by suggesting corrections to fundamental designs on the basis of thorough theoretical understandings.

2. Electromagnetic Modeling

[7] In this work, LP arrays are modelled by perfectly conducting sheets without any further restriction on the geometry. The radiation problem is formulated by using the electric field integral equation (EFIE) that can be written by using the boundary condition for the tangential electric field on the surface as

$$\hat{\boldsymbol{t}} \cdot \int_{S'} d\boldsymbol{r}' \overline{\boldsymbol{G}}(\boldsymbol{r}, \boldsymbol{r}') \cdot \boldsymbol{J}(\boldsymbol{r}') = \frac{i}{k\eta} \hat{\boldsymbol{t}} \cdot \boldsymbol{E}^{inc}(\boldsymbol{r}), \qquad (1)$$

where the scattered electric field is expressed in terms of the radiation integral of the induced (unknown) surface current $\boldsymbol{J}(\boldsymbol{r})$ over the surface of the antenna S'. In (1), $\hat{\boldsymbol{t}}$ is any tangential unit vector on the surface at the observation point $\boldsymbol{r}$, $\boldsymbol{E}^{inc}(\boldsymbol{r})$ is the incident electric field created by the excitation, and

$$\overline{\boldsymbol{G}}(\boldsymbol{r}, \boldsymbol{r}') = \left[\overline{\boldsymbol{I}} + \frac{\nabla\nabla}{k^2}\right] g(\boldsymbol{r}, \boldsymbol{r}') \qquad (2)$$

is the dyadic Green's function based on the scalar Green's function

$$g(\boldsymbol{r}, \boldsymbol{r}') = \frac{e^{ik|\boldsymbol{r}-\boldsymbol{r}'|}}{4\pi|\boldsymbol{r}-\boldsymbol{r}'|} \qquad (3)$$

for the three-dimensional (3-D) Helmholtz equation.

[8] For the numerical solution of the EFIE in (1) by the method of moments (MOM) [*Harrington*, 1993], the unknown surface current $\boldsymbol{J}(\boldsymbol{r})$ is expanded in a series of basis functions $\boldsymbol{b}_n(\boldsymbol{r})$ as

$$\boldsymbol{J}(\boldsymbol{r}) = \sum_{n=1}^{N} a_n \boldsymbol{b}_n(\boldsymbol{r}), \qquad (4)$$

where a_n is the unknown coefficient of the nth basis function. For the radiation problems considered in this paper, the surface of the antennas are triangulated, and the Rao-Wilton-Glisson (RWG) basis functions [*Rao et al.*, 1982] are used to expand the current density. Then,

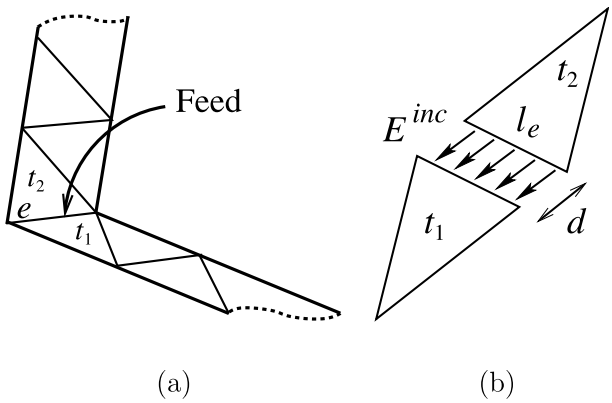

Figure 2. (a) Feed location of the antenna. (b) Delta gap source located on edge e.

the boundary condition is tested by using the inner product of the electric field and testing functions $\boldsymbol{t}_m(\boldsymbol{r})$ so that an $N \times N$ matrix equation is obtained as

$$\sum_{n=1}^{N} Z_{mn} a_n = v_m, \qquad m = 1, .., N, \tag{5}$$

where Z_{mn} is the matrix element derived as

$$Z_{mn} = \int_{S_m} d\boldsymbol{r}\boldsymbol{t}_m(\boldsymbol{r}) \cdot \int_{S_n} d\boldsymbol{r}'\boldsymbol{b}_n(\boldsymbol{r}')g(\boldsymbol{r},\boldsymbol{r}') - \frac{1}{k^2}\int_{S_m} d\boldsymbol{r}\boldsymbol{t}_m(\boldsymbol{r}) \cdot \int_{S_n} d\boldsymbol{r}'\boldsymbol{b}_n(\boldsymbol{r}') \cdot [\nabla\nabla' g(\boldsymbol{r},\boldsymbol{r}')], \tag{6}$$

and v_m is the element of the excitation vector derived as

$$v_m = \frac{i}{k\eta}\int_{S_m} d\boldsymbol{r}\boldsymbol{t}_m(r) \cdot \boldsymbol{E}^{inc}(\boldsymbol{r}). \tag{7}$$

In (6) and (7), S_m and S_n represent the surfaces of the testing and the basis functions, respectively. In compliance with a Galerkin scheme, the testing functions are also chosen as RWG functions. Then, the elements of the symmetric impedance matrix are carefully computed using (6) and employing the singularity extraction techniques [*Graglia*, 1993] for the inner integrals over S_n. In addition, the numerical integrations over S_n and S_m are performed by using adaptive Gaussian quadratures to satisfy a strict limit of maximum 0.5% error.

[9] To excite the antenna, local electric field $\boldsymbol{E}^{inc}(\boldsymbol{r})$ is defined inside the infinitely narrow openings of the delta gap sources placed at the feed locations. As an example, Figure 2 shows a single delta gap source placed at the feed of an antenna located at the edge e between the triangles t_1 and t_2. The incident electric field is defined as

$$\boldsymbol{E}^{inc}(\boldsymbol{r}) = \lim_{d\to 0} \hat{\boldsymbol{u}}\delta(\boldsymbol{r} - \boldsymbol{r}_e)/d, \tag{8}$$

where $\boldsymbol{r}_e$ denotes any point on the edge, $\hat{\boldsymbol{u}}$ is the unit vector on the surface perpendicular to the edge, and d is the width of the theoretical gap as shown in Figure 2b. In the limit $d \to 0$, the gap shrinks to the edge e. The delta function $\delta(\boldsymbol{r} - \boldsymbol{r}_e)$ in (8) indicates that $\boldsymbol{E}^{inc}(\boldsymbol{r})$ is zero outside the small gap. Then, the elements of the excitation vector can be evaluated as

$$v_m = \frac{i}{k\eta}\int_{S_m} d\boldsymbol{r}\boldsymbol{t}_m(\boldsymbol{r}) \cdot \lim_{d\to 0} \hat{\boldsymbol{u}}\delta(\boldsymbol{r} - \boldsymbol{r}_e)/d = \left\{ \begin{array}{ll} \pm\dfrac{il_e}{k\eta} & m = e \\ 0 & \text{otherwise} \end{array} \right\}, \tag{9}$$

where we use the fact that the normal component of the RWG testing function becomes unity on its edge. In (9), l_e represents the length of the edge and the $\pm$ sign for $m = e$ case is determined by the direction of the vector $\hat{\boldsymbol{u}}$ that can be defined arbitrarily. Using the expression in (9), it is obvious that only one element ($m = e$) of the excitation vector will be nonzero.

[10] Finally, the system in (5) is solved with either a direct or an iterative method to find the coefficients for the basis functions. For larger problems involving arrays of several antennas [*Gürel and Ergül*, 2004], the solutions are accelerated by the fast multipole method (FMM) [*Coifman et al.*, 1993] and the multilevel fast multipole algorithm (MLFMA) [*Chew et al.*, 2001]. In these methods, only the near-field interactions are calculated directly as in (6) while the far-field interactions are computed efficiently using diagonalized operators to accelerate the matrix-vector multiplications in an iterative solver.

3. Designs and Simulations

3.1. Theoretical Design of an LP Antenna

[11] In Figure 1, a nonplanar antenna design comprising two planar LP arms with narrow trapezoidal tooth elements is shown with its apex located at the origin. On each arm, the antenna has 22 teeth, alternating from side to side of the constant-width feed line, whose lengths, widths, and distances to the source location are determined according to the log-periodic rules [*DuHamel and Chadwick*, 1984; *Mayes*, 1988]. The tooth sequence does not continue up to the apex location, where the source is located, establishing a toothless part of the feedline to supply the electrical connection. The geometric ratio

$$\tau = \frac{R_{n+1}}{R_n} \tag{10}$$

and the tooth width ratio

$$\varepsilon = \frac{R_n - w_n}{R_n} \tag{11}$$

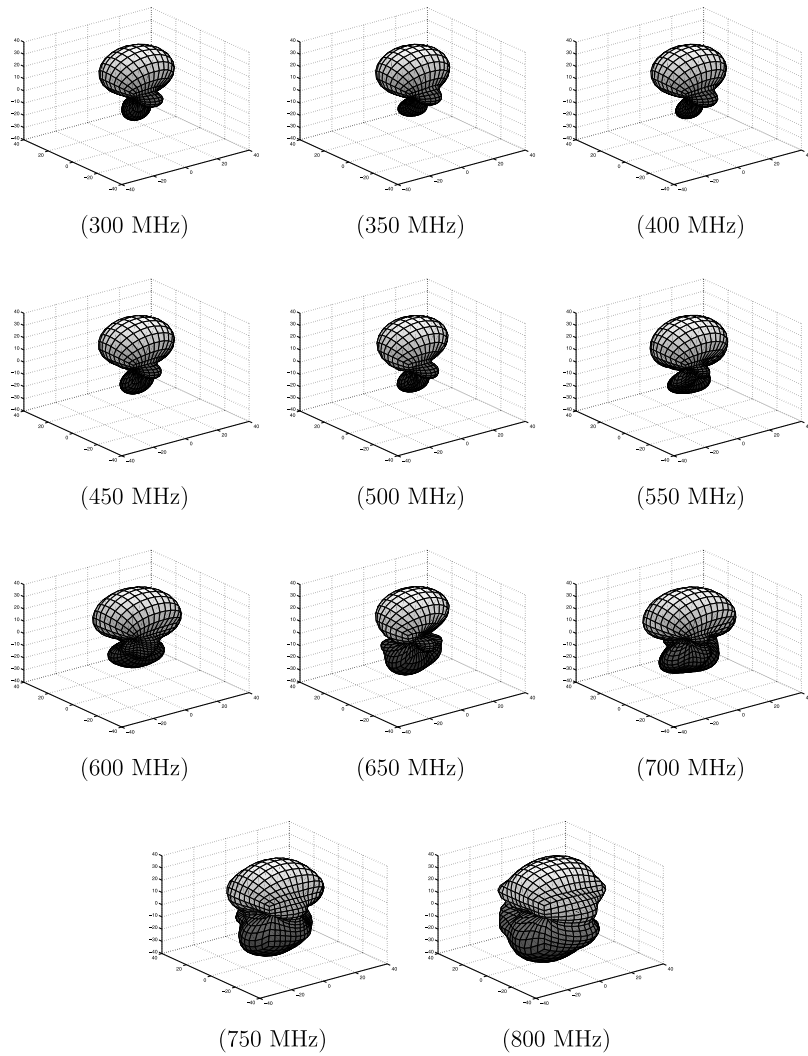

Figure 3. Three-dimensional far-field radiation pattern of the LP antenna design shown in Figure 1 for various frequencies in the 300–800 MHz range. Normalized radiated power is presented in a logarithmic scale.

are selected as $\tau = 0.95$ and $\varepsilon = 0.98$, where R_n is the distance between the source location and the nth tooth, while w_n is the width of the nth tooth. The angle α is 15° so that the arms expand from the source location with an angle of 30°, and the teeth are attached to the center strips with constant widths. If the length of the antenna arms is kept constant, increasing or decreasing the angle α shifts the frequency range of operation to lower or higher frequencies, respectively, since the lengths of the teeth change. On the other hand, if it is desirable to keep the frequency range unchanged, then varying the angle α affects the length of the antenna arm. For this nonplanar design, the angle between the two arms, φ, is chosen as 45°.

[12] This set of parameters differs somewhat from those of the original nonplanar trapezoidal tooth LP antennas [*Isbell*, 1958], resembling more closely those of the LP dipole arrays. The constant-width feedline is also a feature of the original LP dipole arrays. However, the angle between the elements is not zero, as it is for the LP dipole arrays, but a value consistent with the original parameters of the nonplanar trapezoidal tooth LP antennas. Antennas with this geometry have not been studied extensively before, either theoretically or experimentally (P. E. Mayes, private communication, 2004).

[13] The lengths of the smallest and the largest teeth are approximately 9 cm and 27 cm, respectively. It is

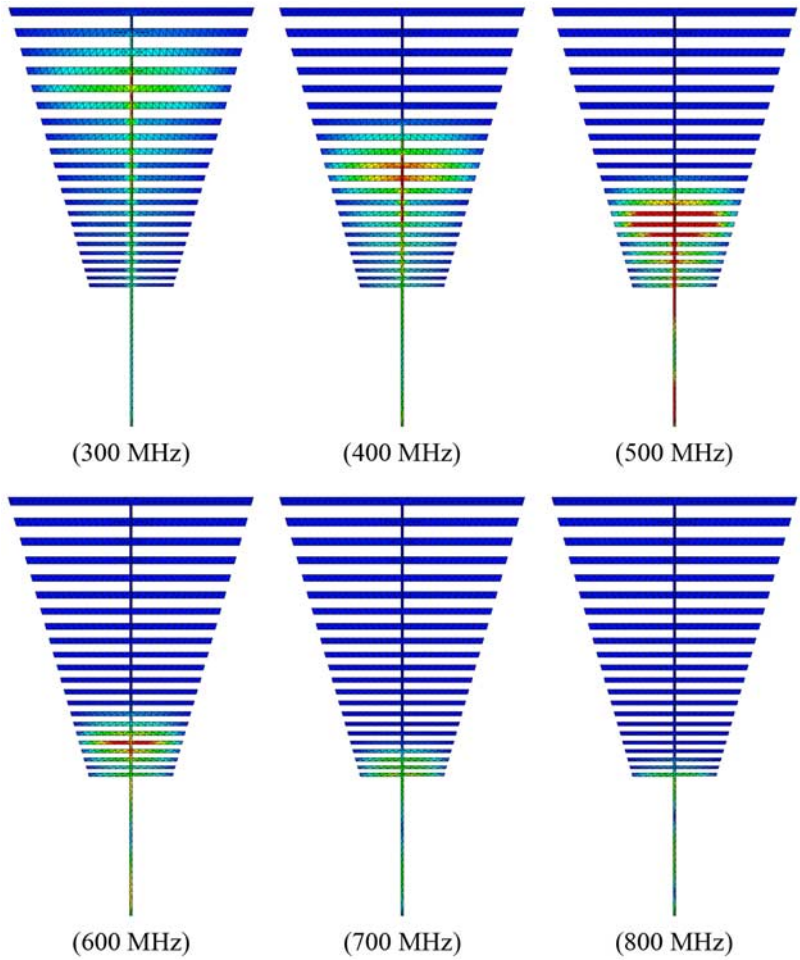

Figure 4. Current distribution on the LP antenna design shown in Figure 1 at different frequencies. Active region is seen to shift as a function of the frequency and spills out of the antenna at high frequencies.

well known that a significant majority of the current on an LP antenna exists in the active region, which resides on the teeth that are about a quarter wavelength long [*Stutzman and Thiele*, 1981; *Kraus*, 1988] so that pairs of quasi-symmetric teeth form half-wavelength-long radiating elements. Then, if the small current outside the active region is ignored, this design is expected to operate nearly frequency-independently in the 300–800 MHz range, provided that the active region is completely accommodated on the antenna. Ignoring many other details, this simple guess does not consider the overflow of the active region due to its finite but unknown width, which could easily be included in the analysis by using the available information if the design was an LP dipole array [*Balanis*, 1997]. However, for the design under consideration, this valuable information can only be obtained through the simulation results.

3.2. Simulations

[14] Figure 3 shows normalized plots of the 3-D far-field radiation pattern of the designed antenna at various frequencies in the 300–800 MHz range. The main beam points in the z direction, along the apex of the antenna, due to backfire radiation. The plots are logarithmically scaled in order to show the details of the radiation patterns. For low frequencies, the radiation pattern seems to be nearly frequency-independent. However, the antenna fails to maintain the same radiation pattern for frequencies above 550 MHz. In other words, the antenna does not operate frequency-independently in the frequency band it is designed for.

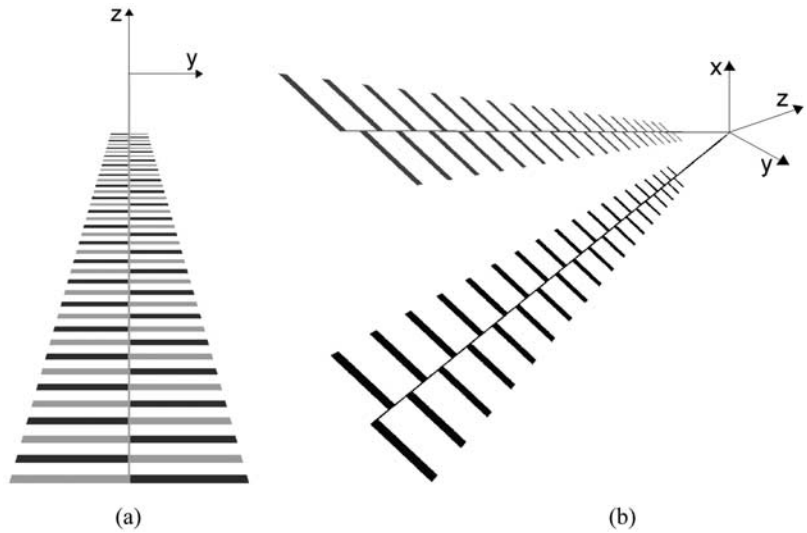

Figure 5. Corrected design with 16 teeth added to each arm of the original antenna shown in Figure 1: (a) top view and (b) three-dimensional view.

[15] Since the radiation pattern of the antenna deteriorates toward the higher end of the frequency band, it is easy to guess that the trouble is associated with the smaller teeth of the antenna. Indeed, the plots of the current distribution at various frequencies shown in Figure 4 demonstrate that the active region spills out of the antenna for higher frequencies. Both the observation and the diagnosis of this problem, which is not predicted by theoretical design rules, are performed in the simulation environment. The solution is also monitored by simulations: extra teeth are added one at a time toward the source end of the antenna until the frequency independence property of the antenna is found satisfactory over the entire 300–800 GHz frequency range. The corrected design with 2×38 teeth is shown in Figure 5, while the radiation pattern and current distribution plots for this design are shown in Figures 6 and 7, respectively. The far-field plots in Figure 6 are nearly frequency-independent in the desired frequency range. The plots of the current distribution in Figure 7 show that the active region is successfully located on the antenna for all frequencies in the desired band, as opposed to the high-frequency spillover demonstrated in Figure 4.

[16] The directive gain in the z direction, which is the intended direction of radiation, is defined as

$$D(\theta = 0) = 4\pi \frac{|E_\theta(\theta = 0)|^2 + |E_\phi(\theta = 0)|^2}{\int_0^{2\pi} \int_0^{\pi} \left[|E_\theta(\theta, \phi)|^2 + |E_\phi(\theta, \phi)|^2 \right] \sin\theta d\theta d\phi}, \quad (12)$$

where E_θ and E_ϕ are the θ and ϕ components, respectively, of the far-zone radiated electric field. For a frequency-independent antenna, the directive gain is expected to remain relatively unchanged over the frequency band of interest. The directive gain curves in Figure 8 clearly demonstrate the improvement in the operation of the modified antenna. Evaluation of the integral in equation (12) is elucidated in Appendix A.

[17] The directive gain is also related to φ, that is, the angle between the arms. Higher values of φ reduce the width of the main beam, but increase the sidelobe level. Lower values of φ suppress the sidelobe lobes, but increase the beam width. Values of φ in the $30°$–$45°$ range are observed to provide a trade-off for high directive gain.

3.3. Design of a Two-Antenna Structure

[18] Having fulfilled the frequency independence property of the trapezoidal tooth LP antenna shown in Figure 5, it would be desirable to add beam-steering capability and improve the relatively low directivity. For this purpose, the two-antenna array illustrated in Figure 9 will be investigated. The two identical antennas, which are similar to the one in Figure 5 with 2×38 teeth and $\alpha = 15°$, but different with $\varphi = 30°$, are separated by $40°$ from center to center. These two antennas can be considered as forming a limited sector of circular array spanning the full $360°$ on the x-y plane.

[19] Circular arrays are thoroughly studied by *Balanis* [1997]. However, the two antennas in Figure 9 are so close to each other that mutual interactions cannot be ignored, rendering the concept of a simple array factor

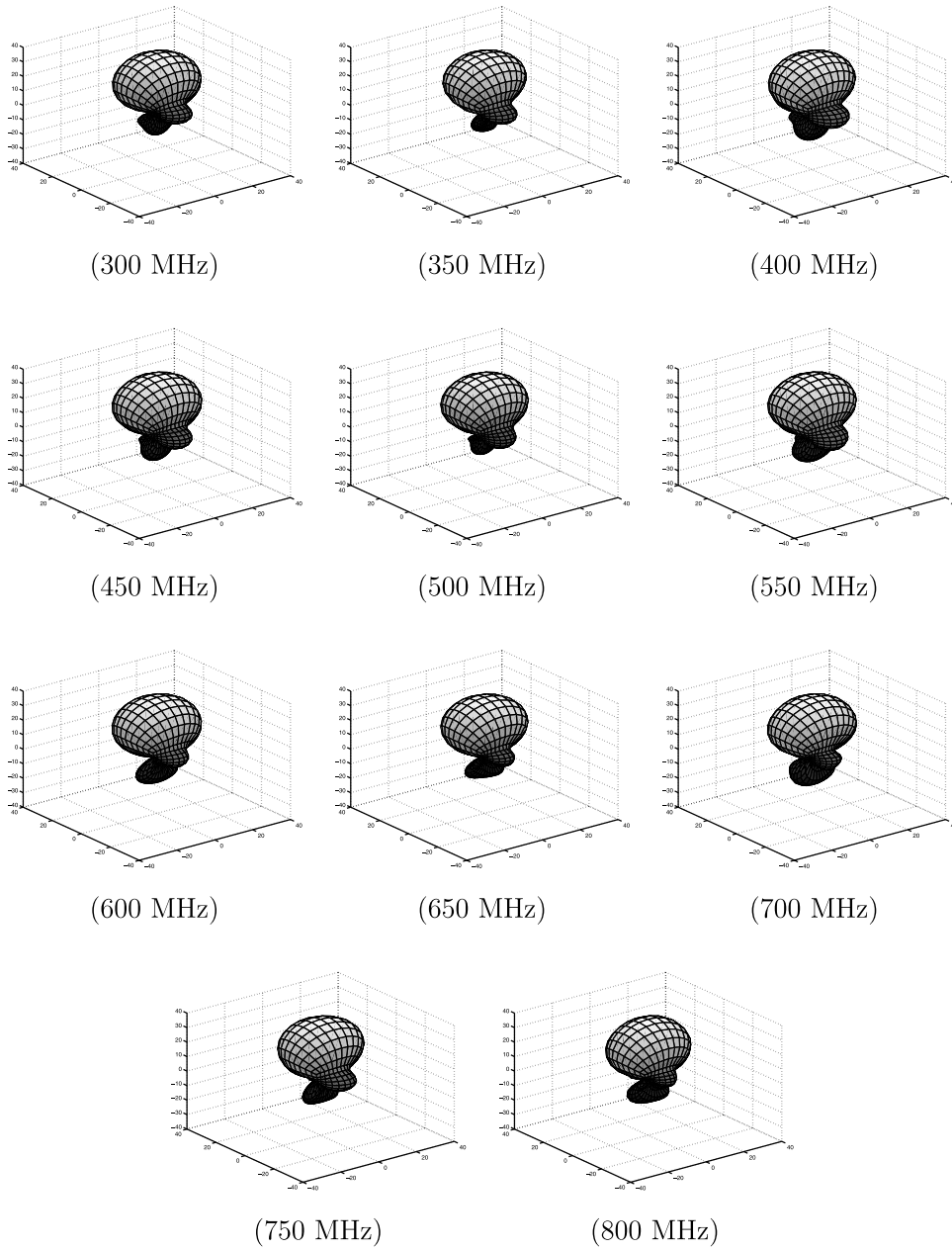

Figure 6. Three-dimensional far-field radiation pattern of the corrected LP antenna design shown in Figure 5.

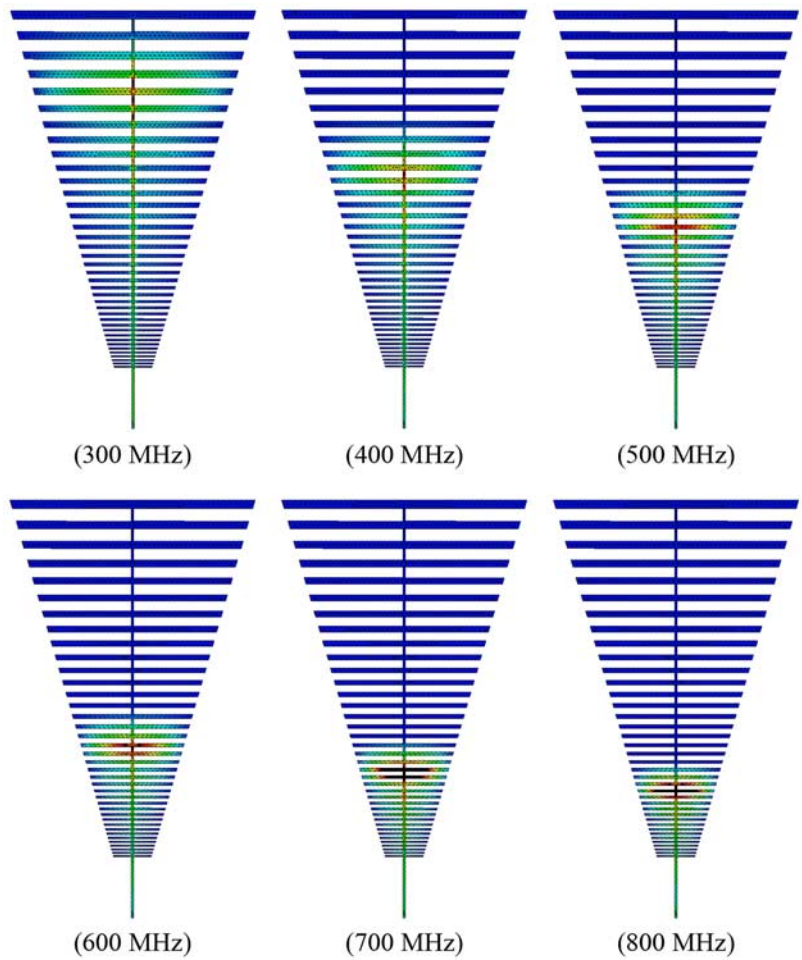

Figure 7. Current distribution on the corrected LP antenna design shown in Figure 5 at different frequencies. Active region is seen to be successfully contained on the antenna for all frequencies.

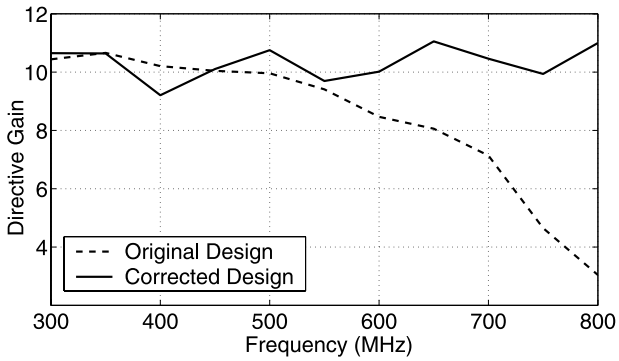

Figure 8. Directive gain in the z direction for the original (dashed curve) and corrected (solid curve) LP antenna designs shown in Figures 1 and 5, respectively.

useless. Therefore a meaningful analysis of the array can only be performed in a simulation environment.

[20] Circular arrangement is essential to assure the frequency independence of the two-antenna configuration—as well as more populous arrays—since frequency-independent antennas should be characterized by angles, and not by distances, which correspond to unequal numbers of wavelengths at different frequencies. For the same reason, the feedline strip is designed to have a constant angle, as opposed to a constant width. Also, in order to avoid the electrical contact of the antennas in the circular configuration, the feedline strips are shortened and the two arms of the antennas are connected by a z-directed conductor, which also incorporates the delta gap excitation.

[21] Because of the symmetric orientation of the array with respect to the x axis, as shown in Figure 9, the main beam is steered around the $-x$ direction. For each selected direction of radiation, complex excitation coefficients of the two antennas are optimized to produce the highest directive gain in that direction. A brute force technique is employed for the optimization since there are only two antennas. Genetic algorithms are used for the optimization of more populous arrays [*Gürel and Ergül*, 2004]. For two antennas, defining $I_1 = A_1 e^{i\psi_1}$ and $I_2 = A_2 e^{i\psi_2}$ as the two complex excitation coefficients at a certain frequency, there are only two independent variables to be optimized, that is, the ratio of the magnitudes of the two excitation coefficients (A_1/A_2) and their phase difference ($\psi_2 - \psi_1$). However, in order to avoid very large values of A_1/A_2 and division by zero, it is more convenient to optimize A_1 and A_2, instead of their ratio. For this purpose, the optimization algorithm sets $\psi_1 = 0$ and samples discrete values of A_1 and A_2 in the interval [0, 1] and ψ_2 in [0, 360°]. Fine discretizations of A_1, A_2, and ψ_2 result in thousands of combinations of I_1 and I_2. For each (I_1, I_2) combination, far-zone electric field $\mathbf{E}(I_1, I_2)$ is found and substituted in equation (12) to compute the directive gain in the desired direction. The brute force optimization algorithm determines the best (I_1, I_2) combination by selecting the highest directive gain among thousands.

[22] The brute force technique can be implemented efficiently by using the linearity of the electromagnetic radiation problem with respect to the sources. Thus $\mathbf{E}(I_1, I_2)$ values do not have to be computed through MOM solutions for thousands of different combinations of (I_1, I_2). Instead, only two MOM solutions to compute

$$\mathbf{E}_1 = \mathbf{E}(I_1 = 1, I_2 = 0) \tag{13}$$

and

$$\mathbf{E}_2 = \mathbf{E}(I_1 = 0, I_2 = 1) \tag{14}$$

are sufficient to easily determine the far-zone electric field

$$\mathbf{E} = I_1\mathbf{E}_1 + I_2\mathbf{E}_2 \tag{15}$$

due to any (I_1, I_2).

[23] Since both the array configuration and the individual antennas are designed to be nearly frequency-independent, the optimization can be performed at a single frequency and the results (e.g., radiation pattern and directive gain) can be expected to remain almost the

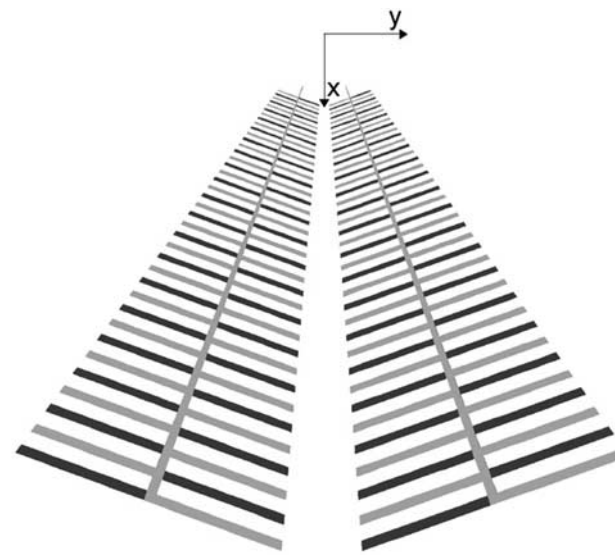

Figure 9. Frequency-independent arrangement of two log-periodic antennas in a circular array configuration, top view.

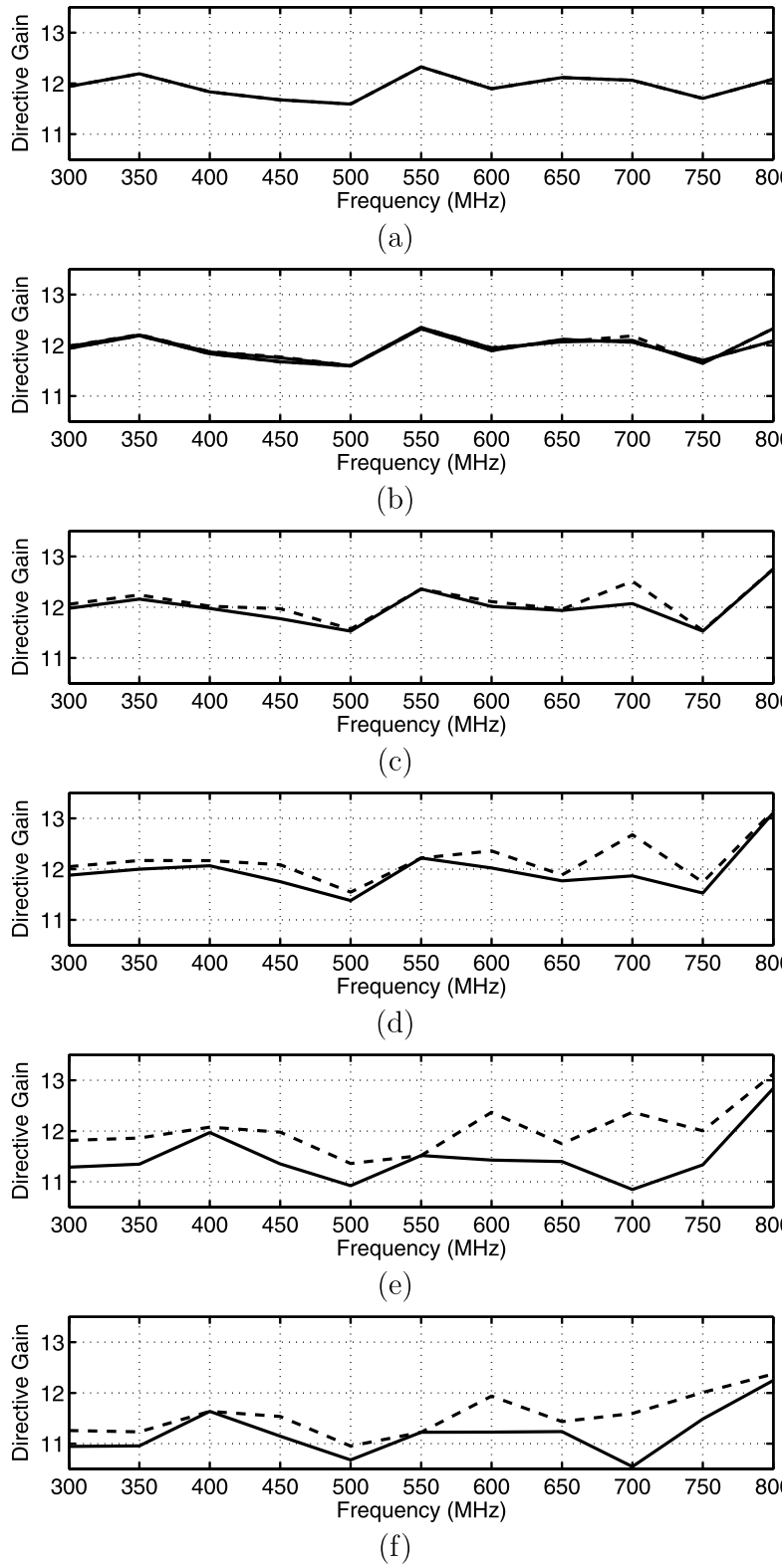
Directive Gain
13
12
11
300 350 400 450 500 550 600 650 700 750 800
Frequency (MHz)
(a)
Directive Gain
13
12
11
300 350 400 450 500 550 600 650 700 750 800
Frequency (MHz)
(b)
Directive Gain
13
12
11
300 350 400 450 500 550 600 650 700 750 800
Frequency (MHz)
(c)
Directive Gain
13
12
11
300 350 400 450 500 550 600 650 700 750 800
Frequency (MHz)
(d)
Directive Gain
13
12
11
300 350 400 450 500 550 600 650 700 750 800
Frequency (MHz)
(e)
Directive Gain
13
12
11
300 350 400 450 500 550 600 650 700 750 800
Frequency (MHz)
(f)

Figure 10

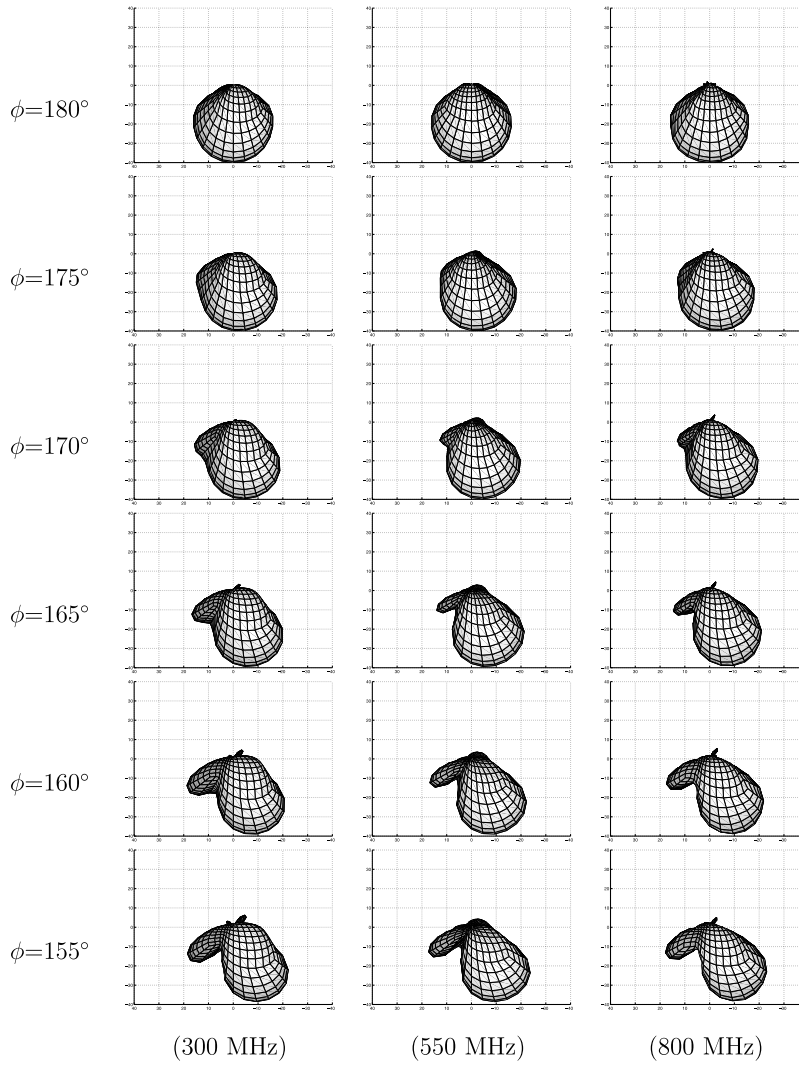

Figure 11. Steering of the normalized far-field radiation pattern of the two-element array in the *y*-*x* plane. For each desired direction of the main beam, the optimizations are performed only at a single frequency of 550 MHz.

same at other frequencies in the 300–800 MHz range. Figure 10 demonstrates the following points:

[24] 1. Directive gain is quite flat over the 300–800 MHz frequency band for various directions of the main beam.

[25] 2. Directive gain of the two-antenna array is consistently higher than that of a single LP antenna shown in Figure 8.

[26] 3. When optimizations are performed at several frequencies that are 50 MHz apart, the results are considerably close to those obtained by optimization at a single frequency (550 MHz).

[27] Figure 11 shows the radiation patterns of the array on the *y*-*x* plane. The optimizations are performed only at 550 MHz. It is demonstrated that the main beam of the array can be steered by optimizing the excitation

Figure 10. Directive gain values for the array in Figure 9 obtained by optimizing the main beam in the direction of $\theta = 90°$ and (a) $\phi = 180°$, (b) $\phi = 175°$, (c) $\phi = 170°$, (d) $\phi = 165°$, (e) $\phi = 160°$, and (f) $\phi = 155°$. The dashed curves show the directive gains obtained by multiple optimizations at different frequencies with 50 MHz interval, while the solid curves show the directive gains obtained by using the source values found with a single optimization at 550 MHz.

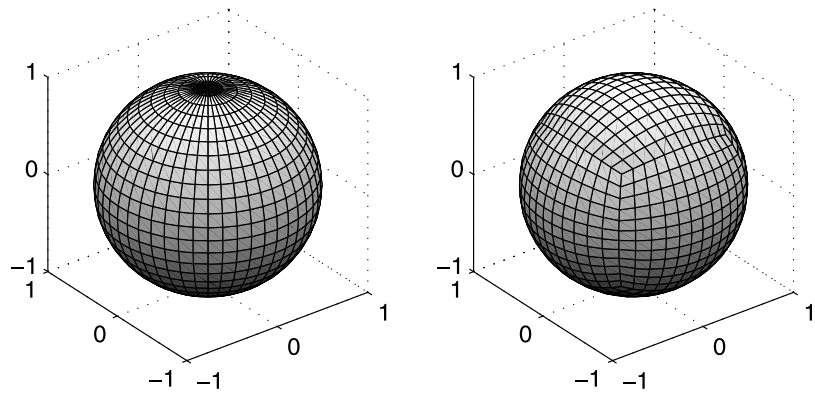

Figure A1. Discretization of the unit sphere: (a) sampling with equally spaced points in the θ-ϕ domain and (b) uniform sampling of six biquadratic patches in the *u*-*v* domain.

coefficients and that this can be achieved in a frequency-independent fashion.

4. Concluding Remarks

[28] Unlike the LP dipole arrays, which have well-known and time-tested theoretical design recipes, more complicated LP antennas require some degree of correction following their theoretical design according to the log-periodic rules. In this paper, nonplanar trapezoidal tooth LP antennas are considered. It is established that an electromagnetic simulation environment can be utilized to test the sufficiency of the original design, devise the necessary corrections, and perform a final check to assure that the performance requirements are satisfied.

[29] Benefits obtained by combining the theoretical wisdom with the power of accurate numerical simulation environments capable of handling arbitrary geometries at various frequencies are further demonstrated by designing a two-element array of trapezoidal tooth LP antennas. The array operates frequency-independently in the same wide frequency band as its elements, exhibits higher directivity than its elements, and has the novel feature of beam steering. Investigation of more populous arrays of LP antennas [*Gürel and Ergül*, 2004] to improve the beam-steering capability while preserving the frequency independence is currently under study.

Appendix A: 3-D Radiation Patterns: Sampling and Integration

[30] In order to plot the 3-D radiation patterns presented in Figures 3, 6, and 11, the far-zone radiation fields of the corresponding antennas shown in Figures 1, 5, and 9 need to be calculated at various directions as a function of the two angular parameters, θ and ϕ. If the unit sphere is sampled with equally spaced points in the θ-ϕ domain, the resulting discretization is illustrated in Figure A1a, where an unnecessary crowding of the sampling points around the north and south poles is observed. Since the shape of the radiation pattern is completely arbitrary, there are no preferred directions requiring denser sampling. Thus not only is the dense sampling around the poles redundant and inefficient (a significant amount of computation is performed for each direction), but also generates misleading (more difficult to read) 3-D pattern plots. As an alternative, the unit sphere is modelled with six biquadratic patches, as shown in Figure A1b. Each biquadratic patch has the general representation of

$$\boldsymbol{r}(u,v) = \sum_{i=0}^{2}\sum_{j=0}^{2} \boldsymbol{a}_{ij} u^i v^j, \tag{A1}$$

where $\boldsymbol{a}_{ij}$'s are vector coefficients and $\boldsymbol{r}(u, v)$ is the position vector from the origin pointing to the surface. Then, the sampling points can be obtained on each patch by uniformly distributing $n \times n$ points in the *u*-*v* domain. Figure A1b illustrates a discretization with 13×13 points on each patch, producing a total of 864 directions on the unit sphere. In contrast, the discretization in Figure A1a, which has comparable fidelity around the equator, contains 33% more sampling directions.

[31] For the calculation of the directive gain in equation (12), the integral in the denominator can be expressed in the *u*-*v* domain for each biquadratic surface as

$$P = \int_{u=0}^{1}\int_{v=0}^{1} \left[|E_\theta(u,v)|^2 + |E_\phi(u,v)|^2\right] \sqrt{g(u,v)}\,du\,dv, \tag{A2}$$

where

$$g(u,v) = g_{uu}(u,v)g_{vv}(u,v) - g_{uv}^2(u,v) \tag{A3}$$

is the determinant of the metric tensor. The first element of this tensor is defined and derived as

$$\begin{aligned} g_{uu}(u,v) &= \frac{\partial \boldsymbol{r}}{\partial u} \cdot \frac{\partial \boldsymbol{r}}{\partial u} \\ &= \sum_{i=0}^{2}\sum_{j=0}^{2} \boldsymbol{a}_{ij} i u^{i-1} v^{j} \cdot \sum_{k=0}^{2}\sum_{l=0}^{2} \boldsymbol{a}_{kl} k u^{k-1} v^{l} \\ &= \sum_{i=1}^{2}\sum_{j=0}^{2} \boldsymbol{a}_{ij} i u^{i-1} v^{j} \cdot \sum_{k=1}^{2}\sum_{l=0}^{2} \boldsymbol{a}_{kl} k u^{k-1} v^{l} \\ &= \sum_{i=1}^{2}\sum_{k=1}^{2}\sum_{j=0}^{2}\sum_{l=0}^{2} \boldsymbol{a}_{ij} \cdot \boldsymbol{a}_{kl} i k u^{i+k-2} v^{j+l}. \end{aligned} \tag{A4}$$

In a similar manner,

$$\begin{aligned} g_{vv}(u,v) &= \frac{\partial \boldsymbol{r}}{\partial v} \cdot \frac{\partial \boldsymbol{r}}{\partial v} \\ &= \sum_{i=0}^{2}\sum_{k=0}^{2}\sum_{j=1}^{2}\sum_{l=1}^{2} \boldsymbol{a}_{ij} \cdot \boldsymbol{a}_{kl} j l u^{i+k} v^{j+l-2} \end{aligned} \tag{A5}$$

and

$$\begin{aligned} g_{uv}(u,v) &= \frac{\partial \boldsymbol{r}}{\partial u} \cdot \frac{\partial \boldsymbol{r}}{\partial v} \\ &= \sum_{i=1}^{2}\sum_{k=0}^{2}\sum_{j=0}^{2}\sum_{l=1}^{2} \boldsymbol{a}_{ij} \cdot \boldsymbol{a}_{kl} i l u^{i+k-1} v^{j+l-1}. \end{aligned} \tag{A6}$$

The functions $g_{uu}(u, v)$, $g_{vv}(u, v)$, and $g_{uv}(u, v)$ can be derived analytically and used to compute the Jacobian in equation (17) for each of the six patches to achieve the evaluation of the integration in equation (12).

[32] **Acknowledgments.** The authors are most grateful to Paul E. Mayes for graciously offering his time and effort to read the whole manuscript and for making invaluable suggestions to improve the manuscript. This work was supported by the Turkish Academy of Sciences in the framework of the Young Scientist Award Program (LG/TUBA-GEBIP/2002-1-12), by the Scientific and Technical Research Council of Turkey (TUBITAK) under research grant 103E008, and by contracts from ASELSAN and SSM.

References

Baker, D. C., and T. G. Reuss (1990), An investigation of the design of a log-periodic dipole array with low side-lobe levels for broadcast applications, *IEEE Trans. Broadcasting*, *36*, 89–93.

Balanis, C. A. (1997), *Antenna Theory*, John Wiley, Hoboken, N. J.

Bell, R. L., C. T. Elfving, and R. E. Franks (1960), Near-field measurements on a logarithmically periodic antenna, *IRE Trans. Antennas Propag.*, *8*, 559–565.

Butson, P. C., and G. T. Thompson (1976), A note on the calculation of the gain of log-periodic dipole antennas, *IEEE Trans. Antennas Propag.*, *24*, 105–106.

Carrel, R. L. (1961), Analysis and design of the log-periodic dipole antenna, *Tech. Rep. 52*, Antenna Lab., Univ. of Ill., Urbana, Ill.

Chew, W. C., J.-M. Jin, E. Michielssen, and J. Song (2001), *Fast and Efficient Algorithms in Computational Electromagnetics*, Artech House, Norwood, Mass.

Coifman, R., V. Rokhlin, and S. Wandzura (1993), The fast multipole method for the wave equation: A pedestrian prescription, *IEEE Antennas Propag. Mag.*, *35*, 7–12.

De Vito, G., and G. B. Stracca (1973), Comments on the design of log-periodic dipole antennas, *IEEE Trans. Antennas Propag.*, *21*, 303–308.

De Vito, G., and G. B. Stracca (1974), Further comments on the design of log-periodic dipole antennas, *IEEE Trans. Antennas Propag.*, *22*, 714–718.

DuHamel, R. H., and G. G. Chadwick (1984), Frequency-independent antennas, in *Antenna Engineering Handbook*, edited by R. C. Jackson and H. Jasik, chap. 14, pp. 24–32, McGraw-Hill, New York.

DuHamel, R. H., and D. E. Isbell (1957), Broadband logarithmically periodic antenna structures, *1957 IRE Natl. Conv. Rec. Part 1*, 119–128.

DuHamel, R. H., and F. R. Ore (1958), Logarithmically periodic antenna designs, *1958 IRE Natl. Conv. Rec. Part 1*, 139–152.

Excell, P. S., A. D. Tinniswood, and R. W. Clarke (1999), An independently fed log-periodic antenna for directed pulsed radiation, *IEEE Trans. Electromagn. Compat.*, *41*, 344–349.

Gong, Z., and K. G. Balmain (1986), Reduction of the anomalous resonances of symmetric log-periodic dipole antennas, *IEEE Trans. Antennas Propag.*, *34*, 1404–1410.

Graglia, R. D. (1993), On the numerical integration of the linear shape functions times the 3-D Green's function or its gradient on a plane triangle, *IEEE Trans. Antennas Propag.*, *41*, 1448–1455.

Gürel, L., and Ö. Ergül (2004), Broadband circular arrays of log-periodic trapezoidal-tooth antennas, research report, Bilkent Univ., Ankara, Turkey.

Hall, P. S. (1986), Multioctave bandwidth log-periodic microstrip antenna array, *Proc. Inst. Electr. Eng.*, *133*, 127–136.

Harrington, R. F. (1993), *Field Computation by Moment Methods*, IEEE Press, Piscataway, N. J.

Hassan, M. A., A. Al Jabri, and K. Al-Hakbani (1991), Point-matching method for reduction of anomalous radiation of log-periodic dipole array, *Electron. Lett.*, *27*, 1315–1317.

Hilbert, R., M. A. Tilston, and K. G. Balmain (1989), Resonance phenomena of log-periodic antennas: Characteristic-mode analysis, *IEEE Trans. Antennas Propag.*, *37*, 1224–1234.

Isbell, D. E. (1958), Nonplanar logarithmically periodic antenna structures, *Tech. Rep. 30*, Antenna Lab., Univ. of Ill., Urbana, Ill.

Isbell, D. E. (1960), Log-periodic dipole arrays, *IRE Trans. Antennas Propag.*, *8*, 260–267.

Jones, K. E., and P. E. Mayes (1969), Continuously scaled transmission lines with applications to log-periodic antennas, *IEEE Trans. Antennas Propag.*, *17*, 2–9.

Kraus, J. D. (1988), *Antennas*, McGraw-Hill, New York.

Kyle, R. H. (1970), Mutual coupling between log-periodic antennas, *IEEE Trans. Antennas Propag.*, *18*, 15–22.

Lee, S. H., and K. K. Mei (1970), Analysis of zigzag antennas, *IEEE Trans. Antennas Propag.*, *18*, 760–764.

Liang, C. S., and Y. T. Lo (1968), A multipole-field study for the multiarm log-spiral antennas, *IEEE Trans. Antennas Propag.*, *16*, 656–664.

Mayes, P. E. (1988), Frequency-independent antennas, in *Antenna Handbook: Theory, Applications, and Design*, edited by Y. T. Lo and S. W. Lee, pp. 1–113, Van Nostrand Reinhold, Hoboken, N. J.

Oakes, C. R., and K. G. Balmain (1973), Optimization of the loop-coupled log-periodic antenna, *IEEE Trans. Antennas Propag.*, *21*, 148–153.

Paul, A., and I. Gupta (1981), An analysis of log-periodic antenna with printed dipoles, *IEEE Trans. Microwave Theory Tech.*, *29*, 114–117.

Peixeiro, C. (1988), Design of log-periodic dipole antennas, *Proc. Inst. Electr. Eng.*, *135*, 98–102.

Rao, S. M., D. R. Wilton, and A. W. Glisson (1982), Electromagnetic scattering by surfaces of arbitrary shape, *IEEE Trans. Antennas Propag.*, *30*, 409–418.

Smith, H. K., and P. E. Mayes (1991), Log-periodic array of dual-feed microstrip patch antennas, *IEEE Trans. Antennas Propag.*, *39*, 1659–1664.

Stutzman, W. L., and G. A. Thiele (1981), *Antenna Theory and Design*, John Wiley, Hoboken, N. J.

Tammen, D. J., J. M. Bowen, and P. E. Mayes (1993), Numerical studies of the sinuous spiral antenna, *1993 IEEE Antennas Propag. Int. Symp. Dig.*, *31*, 446–449.

Tranquilla, J. M., and K. G. Balmain (1983), Analysis of the loop-coupled log-periodic dipole array, *IEEE Trans. Antennas Propag.*, *31*, 253–260.

Wakabayashi, R., K. Shimada, H. Kawakami, and G. Sato (1999), Circularly polarized log-periodic dipole antenna for EMI measurements, *IEEE Trans. Electromagn. Compat.*, *41*, 93–99.

Wolter, J. (1970), Solution of Maxwell's equations for log-periodic dipole antennas, *IEEE Trans. Antennas Propag.*, *18*, 734–740.

Ö. Ergül and L. Gürel, Department of Electrical and Electronics Engineering, Bilkent University, TR-06800, Bilkent, Ankara, Turkey. (ergul@ee.bilkent.edu.tr; lgurel@bilkent.edu.tr)